

**MODELLING AND ANALYSIS OF
COMPLEX ELECTROMAGNETIC
PROBLEMS USING FDTD
SUBGRIDDING IN HYBRID
COMPUTATIONAL METHODS**

K. N. B. RAMLI

Ph.D.

2011

MODELLING AND ANALYSIS OF COMPLEX ELECTROMAGNETIC PROBLEMS USING FDTD SUBGRIDDING IN HYBRID COMPUTATIONAL METHODS

Development of Hybridised Method of Moments, Finite-Difference Time-Domain Method and Subgridded Finite-Difference Time-Domain Method for Precise Computation of Electromagnetic Interaction with Arbitrarily Complex Geometries

KHAIRUN NIDZAM RAMLI
B.Eng., M.Eng.

Submitted for the Degree of
Doctor of Philosophy

School of Engineering, Design and Technology
University of Bradford

2011

Abstract

MODELLING AND ANALYSIS OF COMPLEX ELECTROMAGNETIC PROBLEMS USING FDTD SUBGRIDDING IN HYBRID COMPUTATIONAL METHODS

Development of Hybridised Method of Moments, Finite-Difference Time-Domain Method and Subgridded Finite-Difference Time-Domain Method for Precise Computation of Electromagnetic Interaction with Arbitrarily Complex Geometries

Keywords

Computational Electromagnetics; Method of Moments (MoM); Finite-Difference Time-Domain (FDTD); Quasi-static method; Hybrid computational method; Subgridding; Principle of equivalent sources; Perfectly Matched Layer (PML); Antennas.

The main objective of this research is to model and analyse complex electromagnetic problems by means of a new hybridised computational technique combining the frequency domain Method of Moments (MoM), Finite-Difference Time-Domain (FDTD) method and a subgridded Finite-Difference Time-Domain (SGFDTD) method. This facilitates a significant advance in the ability to predict electromagnetic absorption in inhomogeneous, anisotropic and lossy dielectric materials irradiated by geometrically intricate sources. The Method of Moments modelling employed a two-dimensional electric surface patch integral formulation solved by independent linear basis function methods in the circumferential and axial directions of the antenna wires. A similar orthogonal basis function is used on the end surface and appropriate attachments with the wire surface are employed to satisfy the requirements of current continuity. The surface current distributions on structures which may include closely spaced parallel wires, such as dipoles, loops and helical antennas are computed. The results are found to be stable and showed good agreement with less comprehensive earlier work by others.

The work also investigated the interaction between overhead high voltage transmission lines and underground utility pipelines using the FDTD technique for the whole structure, combined with a subgridding method at points of interest, particularly the pipeline. The induced fields above the pipeline are investigated and analysed.

FDTD is based on the solution of Maxwell's equations in differential form. It is very useful for modelling complex, inhomogeneous structures. Problems arise when open-region geometries are modelled. However, the Perfectly Matched Layer (PML) concept has been employed to circumvent this difficulty. The establishment of edge elements has greatly improved the performance of this method and the computational burden due to huge numbers of time steps, in the order of tens of millions, has been eased to tens of thousands by employing quasi-static methods.

This thesis also illustrates the principle of the equivalent surface boundary employed close to the antenna for MoM-FDTD-SGFDTD hybridisation. It depicts the advantage of using hybrid techniques due to their ability to analyse a system of multiple discrete regions by employing the principle of equivalent sources to excite the coupling surfaces. The method has been applied for modelling human body interaction with a short range RFID antenna to investigate and analyse the near field and far field radiation pattern for which the cumulative distribution function of antenna radiation efficiency is presented. The field distributions of the simulated structures show reasonable and stable results at 900 MHz. This method facilitates deeper investigation of the phenomena in the interaction between electromagnetic fields and human tissues.

Table of Contents

Acknowledgements	i
Acronyms	ii
Symbols	iv
List of Tables	v
List of Figures	vi
Chapter 1: Introduction	
1.1 Background and Motivations	1
1.2 Development History of FDTD	2
1.3 Development History of MoM	5
1.4 State of the Art of the Original Contribution.....	6
1.5 Overview of the Thesis	7
1.6 References	9
Chapter 2: FDTD Technique for Field Truncation	
2.1 Introduction.....	16
2.2 FDTD Updating Stencils	17
2.3 Numerical Dispersion and Stability.....	26
2.4 Incident Wave Source Excitation.....	28
2.4.1 Hard Source Excitation.....	29
2.4.2 Plane Wave Source Excitation.....	30
2.4.2.1 Total/Scattered Field Formulation in 1-D	32
2.4.2.2 Total/Scattered Field Formulation in 3-D	34
2.5 Absorbing Boundary Conditions	41
2.5.1 3-D Berenger's PML	42
2.5.2 3-D PML Numerical Implementations.....	44
2.6 Conclusion	45
2.7 References	45
Chapter 3: Surface Kernel Solution of the Method of Moments	
3.1 Introduction.....	48
3.2 Moment Method Formulation	51
3.3 Evaluation of Impedance Matrix Elements.....	52
3.4 Solution for Singularity.....	58
3.5 Simulation and Results	62
3.6 Conclusion	76

3.7 References	77
----------------------	----

Chapter 4: Quasi-Static Finite-Difference Time-Domain Subgridding Technique

4.1 Introduction.....	81
4.2 Quasi-Static Theorem.....	83
4.3 Plane Wave Solutions.....	86
4.3.1 Plane Wave in Free Space	86
4.3.2 Plane Wave in Lossy Medium.....	87
4.3.3 Plane Wave in Lossless Medium	93
4.4 Modified Berenger's PML.....	94
4.5 Floquet Boundary Condition	96
4.5.1 Two-dimensional TM Case	97
4.5.2 Three-dimensional TM Case	100
4.6 Biological Cell Tissue Modelling.....	105
4.7 Interaction Between OHTL and Buried Pipeline	115
4.7.1 Near Field Simulation	133
4.8 Conclusion	154
4.9 References	155

Chapter 5: Interaction of EM Fields to the Human Body Using Hybrid Computational Method

5.1 Introduction.....	165
5.2 Modified Total/Scattered Field Formulation.....	171
5.2.1 Outside H Surface Method	172
5.2.2 Inside H Surface Method	173
5.2.3 Boundary Field Components Update Equation in 3-D.....	174
5.3 Hybrid MoM-FDTD-SGFDTD Theoretical Formulation.....	177
5.4 Development of the Antenna.....	181
5.5 Hybrid Model Technique	183
5.5.1 Near Field and Far Field Simulation.....	185
5.5.2 Cumulative Distribution Function.....	219
5.6 Conclusion	226
5.7 References	227

Chapter 6: Conclusion and Recommendation for Further Work

6.1 Summary of Thesis	232
6.2 Conclusion	234
6.3 Recommendation for Further Work.....	235
6.4 References	237

Appendix

Acknowledgements

My sincere recognition goes first of all to **Prof. R. A. Abd-Alhameed** and **Prof. P. S. Excell** for their invaluable advices and constructive criticism throughout the completion of this thesis. They have been generous in their time and always a source of ingenuity to me. I have been deeply impressed by their ability to respond to various work and non-work related state of affairs with sensitivity and understanding. I am indebted to **Dr. D. T. W. Liang, Dr. C. H. See** and **Mr. M. B. Child** for their constructive help throughout critical discussions and helpful comments they have provided pertinent to my research work.

I wish to convey my deepest thanks to my father, **Ramli Bandahara** and my mother, **Noorsah Ismail** for their endless support throughout my life and for providing me the chance to reach this far with my studies. I thank them for having faith in me and always inspiring me through calls. In particular, the financial support from **Ministry of Higher Education Malaysia** and my employer, **Universiti Tun Hussein Onn Malaysia (UTHM)** is gratefully acknowledged. I am sure that I have missed people in the list. However, their help was really appreciated and acknowledged.

Lastly, and by no means least, I am grateful for the love and advocate of my wife, **Roziyana Omar** and my children, **Zaki Irfan Khairun Nidzam** and **Zakwan Hazim Khairun Nidzam** for their sacrifice during this often difficult effort and for their endless support towards my career.

Acronyms

1-D	One-dimension
2-D	Two-dimension
3-D	Three-dimension
3G	Third Generation
ABC	Absorbing Boundary Condition
AC	Alternating Current
ADI-FDTD	Alternating Direction Implicit Finite-Difference Time-Domain
BAN	Body Area Networks
CDF	Cumulative Distribution Function
CFL	Courant-Friedrich-Levy
DC	Direct Current
DOP	Direction of Propagation
EMC	Electromagnetic Compatibility
FDTD	Finite-Difference Time-Domain
FEM	Finite-Element Method
FSS	Frequency Selective Surface
GA	Genetic Algorithm
GTD	Geometrical Theory of Diffraction
HF	High Frequency
HSG	Huygens Subgridding
IFA	Incident-field Array
MIMO	Multiple Input Multiple Output
MoM	Method of Moment
MRI	Magnetic Resonance Imaging
MSMoM	Multistrukture Method of Moment
MTR	Multitemporal Resolution
NAG	Numerical Algorithms Group
NMHA	Normal Mode Helical Antenna
OHTL	Overhead High Voltage Transmission Lines
PBG	Photonic Bandgap
PDF	Probability Density Function
PEC	Perfect Electric Conductor
PEE	Partial Eigenfunction Expansion
PML	Perfectly Matched Layer
Q-factor	Quality Factor
RCS	Radar Cross Section
RF	Radio Frequency
RFID	Radio Frequency Identification

RSS	Received Signal Strength
SAR	Specific Absorption Rate
SGFDTD	Subgridded Finite-Difference Time-Domain
TE	Transverse Electric
TE _z	Transverse electric relative to the z -direction (only H_z , E_x , and E_y fields are present)
TEM	Transverse Electromagnetic
TM	Transverse Magnetic
TM _z	Transverse magnetic relative to the z -direction (only E_z , H_x , and H_y fields are present)
UMTS	Universal Mobile Telecommunications System
UTD	Uniform Geometrical Theory of Diffraction
UWB	Ultra Wideband
VIE	Volume Integral Equation
VHF	Very High Frequency
WBSN	Wireless Body Sensor Network
WLAN	Wireless Local Area Network

Symbols

E	Electric field intensity
H	Magnetic field intensity
B	Magnetic flux density
D	Electric flux density
σ^*	Magnetic resistivity
σ	Electric conductivity
μ	Magnetic permeability
ϵ	Electric permittivity
I_j	Basis function for surface current
\mathbf{J}_j	Surface current
\mathbf{E}_i	Incident electric field strength
L	Integro-differential operator
A	Vector potentials
ϕ	Scalar potentials
\mathbf{W}_m	Testing functions
Z	Impedance matrix
V	Excitation vector
$g(R)$	Free-space Green function
R	Distance between observation and source points on wire surface
A	Radius of helix wire
B	Radius of helix wire
P	Pitch distance between helix wire turns
α	Azimuth angle of circumferential cross-section wire
δ	Pitch angle
γ	Axial length of curvilinear patch
\hat{a}_γ	Unit vector in axial surfaces of wire antenna
\hat{a}_{cs}	Unit vector in circumferential surfaces of wire antenna
\hat{a}_r	Unit vectors in radial directions on the end surface of wire antenna
\hat{a}_{ce}	Unit vectors in circumferential directions on the end surface of wire antenna
$f(\gamma)$	Triangular basis functions into the axial direction
$P_{absorbed}$	Absorbed power
$P_{radiated}$	Radiated power

List of Tables

Table 4.1:	Biological cell simulation parameters	112
Table 4.2:	Electrical properties of cubical cell composition at 2450 MHz	113
Table 4.3:	FDTD simulation parameters	130
Table 4.4:	Pipeline parameters	130
Table 4.5:	Material properties	130
Table 5.1:	Simulation parameters	184
Table 5.2:	Input parameters for hybrid method validation	188
Table 5.3:	Human tissues properties at 900 MHz	196

List of Figures

Figure 2.1:	The electric and magnetic field components distribution on the FDTD lattice [6]	24
Figure 2.2:	Relationship between field components: (a) within a quarter of a unit cell, (b) on a plane [6]	24
Figure 2.3:	Space-time chart of the Yee algorithm in a leapfrog arrangement [1]	25
Figure 2.4:	The flow chart of the time stepping FDTD algorithm [3]	26
Figure 2.5:	Variation of the numerical phase velocity with wave propagation angle in two-dimensional FDTD grid [1]	27
Figure 2.6:	Total and scattered field zoning for a generic scattering case [1] ..	31
Figure 2.7:	Total and scattered field components for 1-D FDTD grid	32
Figure 2.8:	Coordinate origins for the calculation of incident field	35
Figure 2.9:	Location of $E_y(\rightarrow)$ and $E_z(\uparrow)$ components in planes $i = i_0$ and $i = i_1$	35
Figure 2.10:	Location of $E_x(\rightarrow)$ and $E_z(\uparrow)$ components in planes $j = j_0$ and $j = j_1$	36
Figure 2.11:	Location of $E_x(\rightarrow)$ and $E_y(\uparrow)$ components in planes $k = k_0$ and $k = k_1$	37
Figure 3.1:	Basic geometry of the helical antenna driven by a voltage source at its centre. The directions of the orthogonal basis or test functions are shown on the right and represent the source or observations points on the wire surface and its ends	54
Figure 3.2:	Point P on a patch of helix wire above the origin	60
Figure 3.3:	The geometry models of two parallel dipoles and loop antennas including the directions of the basis or test functions used; (a) dipoles, (b) loops	63
Figure 3.4:	The input impedance versus frequency for two parallel dipoles separated by 15 mm; solid line: NEC [6], ('ooo' Resistance, 'xxx' Reactance present work)	64

Figure 3.5:	Input impedance at 300 MHz operating frequency of two parallel dipoles of 50 cm length and 5 mm wire radius versus the separated distance between them; ('***', '+++': Present work), ('ooo' and 'xxx': NEC)	65
Figure 3.6:	The normalised magnitudes of the axial and circumferential surface current components of the antenna geometry given in Figure 3.3 separated by 15 mm versus α at $\gamma = 6.25$ cm for axial and $\gamma = 4.6845$ cm for circumferential from the bottom of the dipoles for different operating frequencies: 'xxx' 100 MHz, '***' 300 MHz, 'ooo' 500 MHz; (a) axial component, (b) circumferential component	65
Figure 3.7:	The normalised magnitudes of the axial and circumferential surface current components versus α at similar location as Figure 3.6, for different separated distances between the dipoles at 300 MHz (equivalent half wavelength dipoles with 0.005λ wire radius): (a) axial component, (b) circumferential component. ('ooo': 15 mm, 'xxx': 30 mm, '***': 50 mm, '+++': 100 mm, '□□□':500 mm)	67
Figure 3.8:	The normalised magnitudes of the axial and circumferential surface current components versus α at similar locations as Figure 3.6, for different separated distances between the dipoles at 300 MHz (equivalent to half wavelength dipoles with 0.01λ wire radius): (a) axial component, (b) circumferential component. ('ooo': 30 mm, 'xxx': 50 mm, '***': 100 mm)	68
Figure 3.9:	Power loss ratio of two parallel half wavelength dipoles for various separation distances; 'ooo': wire radius = 0.005λ , 'xxx': wire radius = 0.01λ	68
Figure 3.10:	The normalised magnitudes of the axial and circumferential surface current components versus α at $\phi = 0^\circ$: axial component and $\phi = 33.75^\circ$: circumferential component, for a single loop antenna for different operating frequencies. The loop radius and wire radius are 3 cm and 5 mm respectively. (a) axial component, (b) circumferential component. ('xxx': 400 MHz, 'ooo': 600 MHz, '+++': 800 MHz, '***': 900 MHz)	69
Figure 3.11:	The normalised magnitudes of the axial and circumferential surface current components versus α at $\phi = 0^\circ$: axial component and $\phi = 33.75^\circ$: circumferential component, for two parallel loops separated by 15 mm and each has a radius of 3 cm and 5 mm wire radius versus different operating frequencies. (a) axial component, (b) circumferential component. ('+++': 400 MHz, 'xxx': 600 MHz, '***': 800 MHz, 'ooo': 900 MHz)	69

-
- Figure 3.12: The normalised magnitudes of the axial and circumferential surface current components versus α at $\phi = 0^\circ$: axial component and $\phi = 33.75^\circ$: circumferential component, for two half wavelength parallel loops each of radius 0.0796 wavelength and 0.013 wavelength wire radius, versus the separation distance ' d '. (a) axial component, (b) circumferential component. ('+++': $d = 3a$, 'xxx': $d = 6a$, '***': $d = 20a$, 'ooo': $d = 100a$) 71
- Figure 3.13: The normalised magnitudes of the axial and circumferential surface current components of a half wavelength single turn helix antenna versus α at different positions from the first end of the helix. The helix radius, wire radius and pitch distance are 0.0796λ , 0.013λ and $3a$ respectively. (a) axial component: '***': 0.031λ , 'ooo': 0.125λ , '+++': 0.25λ (b) circumferential component: '***': 0.0156λ , 'ooo': 0.109λ , '+++': 0.234λ 71
- Figure 3.14: The normalised magnitudes of the axial and circumferential surface current components of the same antenna geometry given in Figure 3.12, except that the operating frequency is half than that used in Figure 3.12 (i.e. operating wavelength 2λ). (a) axial component: '***': 0.031λ , 'ooo': 0.125λ , '+++': 0.25λ (b) circumferential component: '***': 0.0156λ , 'ooo': 0.109λ , '+++': 0.234λ 72
- Figure 3.15: The normalised magnitudes of the axial and circumferential surface current components of a half wavelength two turns helix antenna versus α for different pitch distances. The helix radius and wire radius are 0.04λ and 0.006λ respectively. ('ooo': $P = 3a$, '+++': $P = 5a$, 'xxx': $P = 7a$, '***': $P = 9a$) (a) axial component: taken at 0.031λ from the bottom end of the helix. (b) axial component: taken at the centre of the helix. (c) circumferential component: taken at 0.023λ from the bottom end of the helix 72
- Figure 3.16: The normalised magnitudes of the axial and circumferential surface current components of a half wavelength three turns helix antenna versus α for different pitch distances. The helix radius and wire radius are 0.0265λ and 0.004λ respectively. ('ooo': $P = 3a$, '+++': $P = 5a$, 'xxx': $P = 7a$, '***': $P = 9a$) (a) axial component: taken at 0.0294λ from the bottom end of the helix. (b) axial component: taken at the centre of the helix. (c) circumferential component: taken at 0.022λ from the bottom end of the helix 74
- Figure 3.17: The normalised magnitudes of the axial surface current components of a half wavelength four turns helix antenna versus α for different pitch distances. (a) four turns: the helix radius and wire radius are 0.02λ and 0.003λ respectively; (b) five turns: the

	helix radius and wire radius are 0.015λ and 0.002λ respectively ('ooo': $P = 3a$, '+++': $P = 5a$, 'xxx': $P = 7a$, '***': $P = 9a$)	74
Figure 4.1:	General periodic boundary structure in 2-D	98
Figure 4.2:	General infinite periodic structure in 3-D	100
Figure 4.3:	Location of $E_y(\uparrow)$ and $E_z(\rightarrow)$ components in planes $i = i_o$ and $i = i_N$	101
Figure 4.4:	Location of $E_x(\uparrow)$ and $E_z(\rightarrow)$ components in planes $j = j_o$ and $j = j_N$	101
Figure 4.5:	Location of the orthogonal E_z components at the edges due to the normal incident plane wave parallel to z -axis	104
Figure 4.6:	A half-wavelength dipole antenna was used as current source excitation to the subgrid cells. NCGX, NCGY and NCGZ are the number of cells to be subgridded in the direction of x -axis, y -axis and z -axis respectively	109
Figure 4.7:	Stability analysis for different number of subgrid cells in one main FDTD cell	109
Figure 4.8:	3-D view of the basic simulated cubical structures in FDTD computational domain. The direction of propagation (DOP) is in the z -axis	110
Figure 4.9:	New proposed high definition biological tissue model by using modified subgridding FDTD model	111
Figure 4.10:	2-D view of subgridding on a face of a single biological cell (not to scale)	111
Figure 4.11:	Electric field distribution along z -axis through the centre of the cubical cell	113
Figure 4.12:	Modulus of the electric field on xz -plane at intermediate frequency 10 GHz	113
Figure 4.13:	Modulus of the electric field inside subgrid region on xz -plane at intermediate frequency 10 GHz	114
Figure 4.14:	Case 1: The observed field was located inside subgrid area: (a) Without subgrid, (b) With subgrid	119
Figure 4.15:	Case 2: The observed field was located outside subgrid area: (a) Without subgrid, (b) With subgrid	119

Figure 4.16:	Case 1: The electric field in subgrid region (E_{zg}) and at normal grid (E_z): (a) When sinusoidal wave was excited, (b) When gaussian pulse was excited	120
Figure 4.17:	Case 1: The magnetic field in subgrid region (H_{yg}) and at normal grid (H_y): (a) When sinusoidal wave was excited, (b) When gaussian pulse was excited	120
Figure 4.18:	Case 2: The electric field E_z with and without subgrid: (a) When sinusoidal wave was excited, (b) When gaussian pulse was excited	121
Figure 4.19:	Case 2: The magnetic field H_y with and without subgrid: (a) When sinusoidal wave was excited, (b) When gaussian pulse was excited	121
Figure 4.20:	Outline of standard circuit 132 kV steel lattice transmission high voltage suspension towers with normal span of 300 m (not to scale) [54,55]	122
Figure 4.21:	Histogram of soil relative permittivity	124
Figure 4.22:	Cumulative distribution function of soil relative permittivity	124
Figure 4.23:	The main region in the computational domain for 132 kV steel lattice transmission high voltage suspension towers model	126
Figure 4.24:	The subgrid region in the computational domain for 132 kV steel lattice transmission high voltage suspension towers model	126
Figure 4.25:	Outline of standard circuit 275 kV steel lattice transmission high voltage suspension towers with normal span of 365 m (not to scale) [54,55]	128
Figure 4.26:	The main region in the computational domain for 275 kV steel lattice transmission high voltage suspension towers model	129
Figure 4.27:	The subgrid region in the computational domain for 275 kV steel lattice transmission high voltage suspension towers model	129
Figure 4.28:	Outline of standard circuit 400 kV steel lattice transmission high voltage suspension towers with normal span of 300 m (low height construction design, not to scale) [54,55]	131
Figure 4.29:	The main region in the computational domain for 400 kV steel lattice transmission high voltage suspension towers model	132
Figure 4.30:	The subgrid region in the computational domain for 400 kV steel lattice transmission high voltage suspension towers model	132

Figure 4.31:	Three-phase sinusoidal sources driven from 132 kV steel lattice transmission high voltage suspension towers	134
Figure 4.32:	The amplitude of electric field E_{zg} plotted against time inside subgrid region	135
Figure 4.33:	The amplitude of magnetic field H_{yg} and H_{xg} plotted against time inside subgrid region	135
Figure 4.34:	The electric field E_z distribution in the main FDTD grid	136
Figure 4.35:	The magnetic field H_y distribution in the main FDTD grid	136
Figure 4.36:	The magnetic field H_x distribution in the main FDTD grid	136
Figure 4.37:	The electric field E_{zg} distribution in the subgrid section	137
Figure 4.38:	The magnetic field H_{yg} distribution in the subgrid section	137
Figure 4.39:	The magnetic field H_{xg} distribution in the subgrid section	138
Figure 4.40:	The induced electric field E_z at 1.75 m above metallic pipeline	138
Figure 4.41:	The induced magnetic field H_y at 1.75 m above metallic pipeline	139
Figure 4.42:	The induced magnetic field H_x at 1.75 m above metallic pipeline	139
Figure 4.43:	Three-phase sinusoidal sources driven from 275 kV steel lattice transmission high voltage suspension towers	141
Figure 4.44:	The amplitude of electric field E_{zg} plotted against time inside subgrid region	141
Figure 4.45:	The amplitude of magnetic field H_{yg} and H_{xg} plotted against time inside subgrid region	142
Figure 4.46:	The electric field E_z distribution in the main FDTD grid	142
Figure 4.47:	The magnetic field H_y distribution in the main FDTD grid	143
Figure 4.48:	The magnetic field H_x distribution in the main FDTD grid	143
Figure 4.49:	The electric field E_{zg} distribution in the subgrid section	144
Figure 4.50:	The magnetic field H_{yg} distribution in the subgrid section	144
Figure 4.51:	The magnetic field H_{xg} distribution in the subgrid section	145
Figure 4.52:	The induced electric field E_z at 1.75 m above metallic pipeline	145

Figure 4.53:	The induced magnetic field H_y at 1.75 m above metallic pipeline	146
Figure 4.54:	The induced magnetic field H_x at 1.75 m above metallic pipeline	146
Figure 4.55:	Three-phase sinusoidal sources driven from 400 kV steel lattice transmission high voltage suspension towers	148
Figure 4.56:	The amplitude of electric field E_{zg} plotted against time inside subgrid region	148
Figure 4.57:	The amplitude of magnetic field H_{yg} and H_{xg} plotted against time inside subgrid region	149
Figure 4.58:	The electric field E_z distribution in the main FDTD grid	149
Figure 4.59:	The magnetic field H_y distribution in the main FDTD grid	150
Figure 4.60:	The magnetic field H_x distribution in the main FDTD grid	150
Figure 4.61:	The electric field E_{zg} distribution in the subgrid section	151
Figure 4.62:	The magnetic field H_{yg} distribution in the subgrid section	151
Figure 4.63:	The magnetic field H_{xg} distribution in the subgrid section	152
Figure 4.64:	The induced electric field E_z at 1.75 m above metallic pipeline	152
Figure 4.65:	The induced magnetic field H_y at 1.75 m above metallic pipeline	153
Figure 4.66:	The induced magnetic field H_x at 1.75 m above metallic pipeline	153
Figure 5.1:	Overview of the modified total and scattered field region for hybrid method	171
Figure 5.2:	Modified total and scattered field components for one-dimensional FDTD hybrid method (outside H surface method) ...	172
Figure 5.3:	Modified total and scattered field components for one-dimensional FDTD hybrid method (inside H surface method)	173
Figure 5.4:	Hybrid MoM-FDTD-SGFDTD configuration for the single source and scatterer geometries	177
Figure 5.5:	Antenna geometry for linear horizontal polarisation	182
Figure 5.6:	Antenna geometry for linear vertical polarisation	182
Figure 5.7:	Equivalent Huygens surface enclosing the antenna for linear horizontal polarisation	184

Figure 5.8:	Equivalent Huygens surface enclosing the antenna for linear vertical polarisation	185
Figure 5.9:	The location of the antenna in proximity to the human body represented by the black dots	186
Figure 5.10:	The antenna is located at the back of the human. Subgrid cells of $10 \times 10 \times 10$ FDTD cells are taken inside the human body	186
Figure 5.11:	The antenna is located in front of the human. Subgrid cells of $10 \times 10 \times 10$ FDTD cells are taken inside the human body	187
Figure 5.12:	A basic geometry of FDTD-SGFDTD for near and far fields validation	188
Figure 5.13:	Magnitude of E_y and E_z electric field components along z axis at $y=7.2$ cm: Near field E_y ('ooo'), E_z ('xxx'), Far field E_y and E_z ('——')	189
Figure 5.14:	Distribution of the E_z and E_{total} field components in dBs at 7.2 cm away from the sensor using near field method: (a) E_z , (b) E_{total}	189
Figure 5.15:	Distribution of the E_z and E_{total} field components in dBs at 7.2 cm away from the sensor using far field method: (a) E_z , (b) E_{total}	190
Figure 5.16:	Case 1: The observed field was located inside subgrid area: (a) Without subgrid, (b) With subgrid	191
Figure 5.17:	Case 2: The observed field was located outside subgrid area: (a) Without subgrid, (b) With subgrid	192
Figure 5.18:	Case 1: The electric field in subgrid region (E_{zg}) and at normal grid (E_z)	192
Figure 5.19:	Case 1: The magnetic field in subgrid region (H_{yg}) and at normal grid (H_y)	193
Figure 5.20:	Case 2: The electric field E_z with and without subgrid	193
Figure 5.21:	Case 2: The magnetic field H_y with and without subgrid	194
Figure 5.22:	The human body model in xz plane of the computational domain. Cross-section at: (a) $y = 35$, (b) $y = 47$, (c) $y = 55$	197
Figure 5.23:	The human body model in yz plane of the computational domain. Cross-section at: (a) $x = 43$, (b) $x = 67$, (c) $x = 92$	198
Figure 5.24:	The human body model in xy plane of the computational domain. Cross-section at: (a) $z = 14$, (b) $z = 67$, (c) $z = 150$	199

Figure 5.25:	The human body model in xy plane of the computational domain. Cross-section at: (a) $z = 205$, (b) $z = 247$, (c) $z = 300$	199
Figure 5.26:	Subgrid cells composition inside the front of human body at position 1: (a) xy plane, (b) xz plane, (c) yz plane	200
Figure 5.27:	Subgrid cells composition inside the front of human body at position 2: (a) xy plane, (b) xz plane, (c) yz plane	200
Figure 5.28:	Subgrid cells composition inside the front of human body at position 3: (a) xy plane, (b) xz plane, (c) yz plane	200
Figure 5.29:	Subgrid cells composition inside the back of human body at position 1: (a) xy plane, (b) xz plane, (c) yz plane	201
Figure 5.30:	Subgrid cells composition inside the back of human body at position 2: (a) xy plane, (b) xz plane, (c) yz plane	201
Figure 5.31:	Subgrid cells composition inside the back of human body at position 3: (a) xy plane, (b) xz plane, (c) yz plane	201
Figure 5.32:	Electric field distribution for horizontal polarised antenna placed at the front of the human (position 1): (a) xy plane, (b) xz plane, (c) yz plane	202
Figure 5.33:	Electric field distribution in subgrid area for horizontal polarised antenna placed at the front of the human (position 1): (a) xy plane, (b) xz plane, (c) yz plane	202
Figure 5.34:	Electric field distribution for horizontal polarised antenna placed at the front of the human (position 2): (a) xy plane, (b) xz plane, (c) yz plane	203
Figure 5.35:	Electric field distribution in subgrid area for horizontal polarised antenna placed at the front of the human (position 2): (a) xy plane, (b) xz plane, (c) yz plane	203
Figure 5.36:	Electric field distribution for horizontal polarised antenna placed at the front of the human (position 3): (a) xy plane, (b) xz plane, (c) yz plane	204
Figure 5.37:	Electric field distribution in subgrid area for horizontal polarised antenna placed at the front of the human (position 3): (a) xy plane, (b) xz plane, (c) yz plane	204
Figure 5.38:	Electric field distribution for horizontal polarised antenna placed at the back of the human (position 1): (a) xy plane, (b) xz plane, (c) yz plane	205

Figure 5.39:	Electric field distribution in subgrid area for horizontal polarised antenna placed at the back of the human (position 1): (a) xy plane, (b) xz plane, (c) yz plane	205
Figure 5.40:	Electric field distribution for horizontal polarised antenna placed at the back of the human (position 2): (a) xy plane, (b) xz plane, (c) yz plane	206
Figure 5.41:	Electric field distribution in subgrid area for horizontal polarised antenna placed at the back of the human (position 2): (a) xy plane, (b) xz plane, (c) yz plane	206
Figure 5.42:	Electric field distribution for horizontal polarised antenna placed at the back of the human (position 3): (a) xy plane, (b) xz plane, (c) yz plane	207
Figure 5.43:	Electric field distribution in subgrid area for horizontal polarised antenna placed at the back of the human (position 3): (a) xy plane, (b) xz plane, (c) yz plane	207
Figure 5.44:	Electric field distribution for vertical polarised antenna placed at the front of the human (position 1): (a) xy plane, (b) xz plane, (c) yz plane	208
Figure 5.45:	Electric field distribution in subgrid area for vertical polarised antenna placed at the front of the human (position 1): (a) xy plane, (b) xz plane, (c) yz plane	208
Figure 5.46:	Electric field distribution for vertical polarised antenna placed at the front of the human (position 2): (a) xy plane, (b) xz plane, (c) yz plane	209
Figure 5.47:	Electric field distribution in subgrid area for vertical polarised antenna placed at the front of the human (position 2): (a) xy plane, (b) xz plane, (c) yz plane	209
Figure 5.48:	Electric field distribution for vertical polarised antenna placed at the front of the human (position 3): (a) xy plane, (b) xz plane, (c) yz plane	210
Figure 5.49:	Electric field distribution in subgrid area for vertical polarised antenna placed at the front of the human (position 3): (a) xy plane, (b) xz plane, (c) yz plane	210
Figure 5.50:	Electric field distribution for vertical polarised antenna placed at the back of the human (position 1): (a) xy plane, (b) xz plane, (c) yz plane	211

Figure 5.51:	Electric field distribution in subgrid area for vertical polarised antenna placed at the back of the human (position 1): (a) xy plane, (b) xz plane, (c) yz plane	211
Figure 5.52:	Electric field distribution for vertical polarised antenna placed at the back of the human (position 2): (a) xy plane, (b) xz plane, (c) yz plane	212
Figure 5.53:	Electric field distribution in subgrid area for vertical polarised antenna placed at the back of the human (position 2): (a) xy plane, (b) xz plane, (c) yz plane	212
Figure 5.54:	Electric field distribution for vertical polarised antenna placed at the back of the human (position 3): (a) xy plane, (b) xz plane, (c) yz plane	213
Figure 5.55:	Electric field distribution in subgrid area for vertical polarised antenna placed at the back of the human (position 3): (a) xy plane, (b) xz plane, (c) yz plane	213
Figure 5.56:	Far field pattern for horizontal polarised antenna placed at the front of the human (position 1): (a) xy plane, (b) xz plane, (c) yz plane; ‘o-o-o’: E_{θ} , ‘x-x-x’: E_{ϕ}	215
Figure 5.57:	Far field pattern for horizontal polarised antenna placed at the front of the human (position 2): (a) xy plane, (b) xz plane, (c) yz plane; ‘o-o-o’: E_{θ} , ‘x-x-x’: E_{ϕ}	215
Figure 5.58:	Far field pattern for horizontal polarised antenna placed at the front of the human (position 3): (a) xy plane, (b) xz plane, (c) yz plane; ‘o-o-o’: E_{θ} , ‘x-x-x’: E_{ϕ}	215
Figure 5.59:	Far field pattern for horizontal polarised antenna placed at the back of the human (position 1): (a) xy plane, (b) xz plane, (c) yz plane; ‘o-o-o’: E_{θ} , ‘x-x-x’: E_{ϕ}	216
Figure 5.60:	Far field pattern for horizontal polarised antenna placed at the back of the human (position 2): (a) xy plane, (b) xz plane, (c) yz plane; ‘o-o-o’: E_{θ} , ‘x-x-x’: E_{ϕ}	216
Figure 5.61:	Far field pattern for horizontal polarised antenna placed at the back of the human (position 3): (a) xy plane, (b) xz plane, (c) yz plane; ‘o-o-o’: E_{θ} , ‘x-x-x’: E_{ϕ}	216
Figure 5.62:	Far field pattern for vertical polarised antenna placed at the front of the human (position 1): (a) xy plane, (b) xz plane, (c) yz plane; ‘o-o-o’: E_{θ} , ‘x-x-x’: E_{ϕ}	217

Figure 5.63:	Far field pattern for vertical polarised antenna placed at the front of the human (position 2): (a) xy plane, (b) xz plane, (c) yz plane; ‘o-o-o’: E_θ , ‘x-x-x’: E_ϕ	217
Figure 5.64:	Far field pattern for vertical polarised antenna placed at the front of the human (position 3): (a) xy plane, (b) xz plane, (c) yz plane; ‘o-o-o’: E_θ , ‘x-x-x’: E_ϕ	217
Figure 5.65:	Far field pattern for vertical polarised antenna placed at the back of the human (position 1): (a) xy plane, (b) xz plane, (c) yz plane; ‘o-o-o’: E_θ , ‘x-x-x’: E_ϕ	218
Figure 5.66:	Far field pattern for vertical polarised antenna placed at the back of the human (position 2): (a) xy plane, (b) xz plane, (c) yz plane; ‘o-o-o’: E_θ , ‘x-x-x’: E_ϕ	218
Figure 5.67:	Far field pattern for vertical polarised antenna placed at the back of the human (position 3): (a) xy plane, (b) xz plane, (c) yz plane; ‘o-o-o’: E_θ , ‘x-x-x’: E_ϕ	218
Figure 5.68:	Histogram of horizontal polarised antenna located at the front of the human for: (a) radiation efficiency, (b) $P_{absorbed} / P_{radiated}$	220
Figure 5.69:	Histogram of horizontal polarised antenna located at the back of the human for: (a) radiation efficiency, (b) $P_{absorbed} / P_{radiated}$	221
Figure 5.70:	Cumulative distribution function of horizontal polarised antenna located at the front and back of the human for: (a) radiation efficiency, (b) $P_{absorbed} / P_{radiated}$	221
Figure 5.71:	Histogram (front and back combination) of horizontal polarised antenna for: (a) radiation efficiency, (b) $P_{absorbed} / P_{radiated}$	222
Figure 5.72:	Cumulative distribution function (front and back combination) of horizontal polarised antenna for: (a) radiation efficiency, (b) $P_{absorbed} / P_{radiated}$	222
Figure 5.73:	Histogram of vertical polarised antenna located at the front of the human for: (a) radiation efficiency, (b) $P_{absorbed} / P_{radiated}$	223
Figure 5.74:	Histogram of vertical polarised antenna located at the back of the human for: (a) radiation efficiency, (b) $P_{absorbed} / P_{radiated}$	223

Figure 5.75:	Cumulative distribution function of vertical polarised antenna located at the front and back of the human for: (a) radiation efficiency, (b) $P_{absorbed} / P_{radiated}$	224
Figure 5.76:	Histogram (front and back combination) of vertical polarised antenna for: (a) radiation efficiency, (b) $P_{absorbed} / P_{radiated}$	224
Figure 5.77:	Cumulative distribution function (front and back combination) of vertical polarised antenna for: (a) radiation efficiency, (b) $P_{absorbed} / P_{radiated}$	225
Figure 6.1:	Comparison between subgridding method: (a) Normal subgridding, (b) Non-uniform mesh, (c) Lobatto cell method	236

Chapter 1

Introduction

1.1 Background and Motivations

Over the past years, a number of numerical and analytical approaches to Maxwell's time-dependent curl equations were broadly used with the increases in computer memory capacity and relentless advances in computational imitating efficiency. Consequently, the demand for efficient field modelling tools in electromagnetic scattering problems is ceaselessly expanding. In general, computational electromagnetic techniques have been applied to vast areas including the study of the radiation, scattering and penetration of electromagnetic wave with 3-D objects, in problems related to telecommunication, electromagnetic compatibility (EMC), microwave devices, waveguide structures and medical diagnosis.

Apparently, many considerations need to be taken into account when deciding to choose the most suitable numerical technique in order to solve a specific problem. Some of the main factors include the geometry of the scattering and radiating objects, computer requirements, the domain of interest whether time-domain or frequency-domain, and the absorbing boundary conditions (ABC). The material characteristics and its geometry play important roles in choosing the approach used to mathematically model the

properties of the electromagnetic interaction. In biomedical application for instance, the object is inhomogeneous, anisotropy, penetrable body which cannot be easily included in the formulations. However, the ability of FDTD algorithm to simulate and investigate the inhomogeneous, anisotropy media makes it very useful and effective technique thus far. Typically, there are two main categories of numerical algorithms approaches applied by researches. They are namely the frequency-domain integral formulation using the Method of Moments (MoM), and the time-domain differential formulation by means of the Finite-Difference Time-Domain (FDTD) method and the Finite Element Method (FEM). Integro-differential equation method is generally global in nature so that the initial and boundary conditions must be imposed as the algorithm continues. In contrast, differential-equation technique is typically local in nature so that the initial and boundary conditions are both directly included in the computational algorithm. The former technique usually postulates extensive analytical pre-processing whereas the later demands negligible analytical pre-processing. The methods mentioned above can be applied to certain specific geometries of concern. Consequently, the differential-equation formulations are increasingly well-known due to the fact that it can solve any type of geometries in the problem space of the computational domain.

1.2 Development History of FDTD

First introduced by Yee in 1966 [1], FDTD is widely used to solve electromagnetic scattering problems due to its muscular characteristics including:

- **Simplicity:** The second-order accurate central finite-difference approximations for spatial and temporal derivatives of the electric and magnetic vector field

components is directly used to solve Maxwell's equations explicitly in the absence of linear algebra.

- **Fidelity:** Wideband and narrowband applications can be easily implemented by applying different type of time pulse shape such as Gaussian and sinusoidal wave respectively.
- **Robustness:** Numerical dispersions in FDTD computations can be enclosed to model very large variety of electromagnetic scattering problems accurately. Furthermore, the FDTD algorithm can be easily implemented on parallel computers for faster simulation time.
- **Effectiveness:** Problems involving nonlinear media can be inherently alleviated in a straightforward manner in the time-domain compared with those in the frequency-domain technique.
- **Versatility:** It can intrinsically be used to model inhomogeneous, anisotropy materials such as biological tissues, geophysical strata and shielding metal structures.

Generally, the algorithm used by Yee was described by the electric field component which was spatially and temporally offset from the magnetic field component to acquire the update equations. These equations were used in a leap-frog manner to propagate the electric and magnetic fields ahead in time. The equations provide the present fields in terms of the past fields all over the computational domain. After Yee's publication, the approach was widely used with different endeavour [2-6].

The boundaries of the computational domain in FDTD need to be carefully treated when

simulating problems in open regions. Spurious reflections will generally occur from the termination of the grid. The problem can be solved by means of the well known method called the absorbing boundary condition (ABC). It is generally meant to absorb any outgoing propagating waves without ideally producing spurious reflections. The ABCs was first proposed in 1971 by Merewether [7] to solve the open region difficulties. The development chronicle to magnify the practicability study of the technique was continued in the literature by [8-12] which were based of nonmaterial type. In contrast, Berenger presented a new idea in 1994 called the perfectly matched layer (PML) ABC which was based on material category [13]. The state of the art of Berenger's PML contributes to notably better precision when compared to the other ABCs in the written works [14, 15] for broad assortment of applications.

The main handicap of FDTD lies in the truth that only consistent grids can be used. Accordingly, the geometry resemblance in FDTD is restricted to staircase-shaped boundaries which lead to a large number of computer memory requirements and the CPU time particularly when dealing with curvature geometries with fine features [16]. The total number of cells in the computational domain grows significantly due to a global fine mesh. Another FDTD weakness is the presence of error due to numerical dispersion [17, 18]. In this case, many scientists were prompted to examine the subgridding scheme as an approach to parry the problem. A variety of methods have been proposed to boost the efficiency of FDTD technique such as non-uniform meshing [19], sub-cellular technique [20], non-orthogonal meshing [21], alternative direction implicit (ADI) method [22-24], higher-order technique [25, 26], hybrid method [27-29] and subgridding method [30-34]. In FDTD subgridding technique, the smaller size

components in a structure is filled with fine grids and the remaining of the space is represented by coarse grids. The fields on the boundary between coarse and fine grids are basically unknown in nature. They are predicted by using spatial and temporal interpolations. The regions of the coarse and fine grids are computed by the FDTD method and are kept in time step which satisfy the Courant stability condition. Consequently, the stable subgridding algorithm can refine the mesh locally. Hence, the accuracy of the solution can be improved without increasing the computational efforts significantly.

1.3 Development History of MoM

The MoM is basically a general procedure for solving linear equations. The “moments” in its name is due to the process of taking moments by multiplying the suitable weighting functions and integrating. In other words, it is essentially the technique of weighted residuals applicable for solving both the differential and integral equations. The advantages of MoM are accuracy, versatility and the potential to compute the near and far zone parameters. Furthermore, the method proved its ability to solve real complex antenna geometry in both frequency and time domain. The use of MoM and related matrix methods has become widespread in electromagnetic areas since the published paper of Richmond in 1965 [35] by generating a system of linear equations for the unknown current density and enforcing the boundary conditions at discrete points in the scattering body. Afterwards, he developed a point-matching solution for scattering by conducting bodies of arbitrary shape [36]. In 1967, Harrington documented the mathematical concept of MoM by which the functional equations of the

field theory were reduced to matrix equations [37]. Later, he published a book on MoM which was a step forward towards the development of the numerical techniques [38].

The prime drawback of using MoM lies beneath its rectangular and triangular basis function. Their usage to examine the problem of electromagnetic scattering by dielectric objects with high dielectric constant leads to spurious charges. This problem was alleviated by means of solenoidal basis function [39, 40]. Wilton and Govind [41] made an effort to circumvent the error currents and anomaly behaviour of the solution near the edges by means of triangle expansion functions with suitable singular pulses at the edges.

The MoM has been favourably employed in variety of electromagnetic applications such as scattering problems [42-45], synthesis of slotted waveguide array antenna [46], field analysis in circular-loop antenna [47, 48], the solution for patch antenna using volume integral equation (VIE) [49], VHF propagation modelling [50] and microwave tomography system [51].

1.4 State of the Art of the Original Contribution

The dominant focus of the research work is the modelling and analysis of the complex electromagnetic problems by means of subgridded FDTD (SGFDTD) scheme to be employed in several applications. In order to achieve the research goal, the basic idea is to use the hybridisation of SGFDTD with MoM in which the tools for electromagnetic field modelling problems can be designed with more accuracy and efficiency. The

surface kernel solution of MoM technique is derived. The method is used to predict the surface current distributions on structures with closely spaced parallel wires, such as dipoles, loops and helical antennas. Next, the present work is devoted to mathematical modelling and implementing SGFDTD in 2-D Cartesian coordinate keeping minimum reflection at the boundary. This method is applied to the interaction between overhead transmission lines to the underground pipeline for validation purposes. The SGFDTD formulation is then embedded inside the hybrid MoM-FDTD method. The full code with the adaptation of subgridding inside the hybrid MoM-FDTD design problems is written in Fortran 90 as a platform. The hybridisation of MoM-FDTD-SGFDTD code is used to analyse and investigate the applications in electromagnetic problems for validation such as the interaction between EM fields to the human body.

1.5 Overview of the Thesis

Chapter 1 postulates historical background and literature survey of FDTD and MoM techniques used to solve electromagnetic scattering issues. It should be noted that a more detailed review of existing literature is reported at the beginning of each chapter with separate references at the end.

Chapter 2 unfolds the theoretical concept of FDTD principles including the derivation of the magnetic and electric field update equations, parameters that control the stability and accuracy, plane wave source modelling concept by applying the equivalent surface, and finally the implementation of Berenger's PML absorbing boundary condition.

Chapter 3 presents the surface kernel solution of the Method of Moments. The surface current distributions on structures with closely spaced parallel wires, such as dipoles, loops and helical antennas, are computed by using the method of moments with a general surface patch formulation. The modelling method employed a two-dimensional electric surface patch integral equation formulation solved by independent piecewise-linear basis function methods in the circumferential and axial directions of the wire.

Chapter 4 explains the modelling and analysis of quasi-static FDTD subgridding technique in two-dimensional approach. The method has been applied to model biological cell with floquet theorem. The interaction between overhead transmission lines and underground pipeline at power-line frequency is also modelled for validation. FDTD technique is used for the whole structure spatial problem combined with subgrid method at the pipeline. The soil in the common corridor has been designed as arbitrarily inhomogeneous.

Chapter 5 describes the hybridisation MoM-FDTD-SGFDTD computational method. The modelling on multiple-region hybrid techniques with frequency-domain MoM and time-domain FDTD and subgridding are suggested and investigated. The method is validated for near field and far field applications particularly on the interaction between electromagnetic fields and human body in which the RFID antenna is located and moved at several positions in front and back of inhomogeneous human body model.

Chapter 6 summarises the overall conclusions and recommendations for further work on related topics.

1.6 References

- [1] K. S. Yee, "Numerical solution of initial boundary value problems involving Maxwell's equations in isotropic media," *IEEE Transactions on Antennas and Propagation*, vol. AP-14, pp. 302-307, 1966.
- [2] A. Taflove and M. E. Brodwin, "Numerical solution of steady-state electromagnetic scattering problems using the time-dependent maxwell's equations," *IEEE Transactions on Microwave Theory and Techniques*, vol. 23, pp. 623-630, 1975.
- [3] A. Taflove and M. E. Brodwin, "Computation of the electromagnetic fields and induced temperatures within a model of the microwave-irradiated human eye," *IEEE Transactions on Microwave Theory and Techniques*, vol. 23, pp. 888-896, 1975.
- [4] R. Holland, "THREDE: A free-field EMP coupling and scattering code," *IEEE Transactions on Nuclear Science*, vol. NS-24, pp. 2416-2421, 1977.
- [5] K. S. Kunz and K. M. Lee, "A three-dimensional finite-difference solution of the external response of an aircraft to a complex transient EM environment: Part I- The method and its implementation," *IEEE Transactions on Electromagnetic Compatibility*, vol. EMC-20, pp. 328-333, 1978.
- [6] A. Taflove, "Application of the finite-difference time-domain method to sinusoidal steady-state electromagnetic-penetration problems," *IEEE Transactions on Electromagnetic Compatibility*, vol. EMC-22, pp. 191-202, 1980.
- [7] D. E. Merewether, "Transient currents induced on a metallic body of revolution by an electromagnetic pulse," *IEEE Transactions on Electromagnetic Compatibility*, vol. EMC-13, pp. 41-44, 1971.

-
- [8] B. Engquist and A. Majda, "Absorbing boundary conditions for numerical simulation of waves," *Applied Mathematical Sciences*, vol. 74, pp. 1765-1766, 1977.
- [9] G. Mur, "Absorbing boundary conditions for the finite-difference approximation of the time-domain electromagnetic-field equations," *IEEE Transactions on Electromagnetic Compatibility*, vol. EMC-23, pp. 377-382, 1981.
- [10] Z. P. Liao, H. L. Wong, B. P. Yang, and Y. F. Yuan, "A transmitting boundary for transient wave analysis," *Scientia Sinica (Series A)*, vol. XXVII, pp. 1063-1076, 1984.
- [11] R. G. Keys, "Absorbing boundary conditions for acoustic media," *Geophysics*, vol. 50, pp. 892-902, 1985.
- [12] R. L. Higdon, "Absorbing boundary conditions for difference approximations to the multi-dimensional wave equation," *Mathematics of Computation*, vol. 47, pp. 437-459, 1986.
- [13] J. P. Berenger, "A perfectly matched layer for the absorption of electromagnetic waves," *Journal of Computational Physics*, vol. 114, pp. 185-200, 1994.
- [14] D. T. Prescott and N. V. Shuley, "Reflection analysis of FDTD boundary conditions - Part I: Time-space absorbing boundaries," *IEEE Transactions on Microwave Theory and Techniques*, vol. 45, pp. 1162-1170, 1997.
- [15] D. T. Prescott and N. V. Shuley, "Reflection analysis of FDTD boundary conditions - Part II: Berenger's PML absorbing layers," *IEEE Transactions on Microwave Theory and Techniques*, vol. 45, pp. 1171-1178, 1997.

-
- [16] A. Akyurtlu, D. H. Werner, V. Veremey, D. J. Steich, and K. Aydin, "Staircasing errors in FDTD at an air-dielectric interface," *IEEE Microwave and Guided Wave Letters*, vol. 9, pp. 444-446, 1999.
- [17] J. B. Schneider and C. L. Wagner, "FDTD dispersion revisited: Faster-than-light propagation," *IEEE Microwave and Guided Wave Letters*, vol. 9, pp. 54-56, 1999.
- [18] J. Represa, C. Pereira, M. Panizo, and F. Tadeo, "A simple demonstration of numerical dispersion under FDTD," *IEEE Transactions on Education*, vol. 40, pp. 98-102, 1997.
- [19] R. Wu, G. Benqing, and Y. Shiming, "An improved method in FDTD simulation to reduce reflection from non-uniform mesh," *3rd International Conference on Microwave and Millimeter Wave Technology Proceedings*, pp. 646-649, 2002.
- [20] S. Kapoor, "Sub-cellular technique for finite-difference time-domain method," *IEEE Transactions on Microwave Theory and Techniques*, vol. 45, pp. 673-677, 1997.
- [21] P. Thoma and T. Weiland, "Numerical stability of finite difference time domain methods," *IEEE Transactions on Magnetics*, vol. 34, pp. 2740-2743, 1998.
- [22] T. Namiki, "A new FDTD algorithm based on alternating-direction implicit method," *IEEE Transactions on Microwave Theory and Techniques*, vol. 47, pp. 2003-2007, 1999.
- [23] F. H. Zheng, Z. Z. Chen, and J. Z. Zhang, "Toward the development of a three-dimensional unconditionally stable finite-difference time-domain method," *IEEE Transactions on Microwave Theory and Techniques*, vol. 48, pp. 1550-1558, 2000.

-
- [24] B. K. Huang, Y. S. Jiang, and W. B. Wang, "A hybrid 2-D ADI-FDTD subgridding scheme," *IEEE International Symposium on Antennas, Propagation and EM Theory Proceedings*, pp. 707-710, 2003.
- [25] M. F. Hadi and M. P. May, "A modified FDTD (2,4) scheme for modeling electrically large structures with high-phase accuracy," *IEEE Transactions on Antennas and Propagation*, vol. 45, pp. 254-264, 1997.
- [26] Z. H. Shao, Z. X. Shen, Q. Y. He, and G. W. Wei, "A generalized higher order finite-difference time-domain method and its application in guided-wave problems," *IEEE Transactions on Microwave Theory and Techniques*, vol. 51, pp. 856-861, 2003.
- [27] G. Cerri, P. Russo, A. Schiavoni, G. Tribellini, and P. Bielli, "MoM-FDTD hybrid technique for analysing scattering problems," *Electronic Letters*, vol. 34, pp. 438-440, 1998.
- [28] A. Monorchio and R. Mittra, "A hybrid finite-element finite-difference time-domain (FE/FDTD) technique for solving complex electromagnetic problems," *IEEE Microwave and Guided Wave Letters*, vol. 8, pp. 93-95, 1998.
- [29] N. V. Venkatarayalu, Y. B. Gan, R. Lee, and L. W. Li, "Antenna modeling using stable hybrid FETD-FDTD method," *Proceedings of 2007 International Symposium on Antennas and Propagation, Honolulu, USA*, pp. 3736-3739, 2007.
- [30] S. S. Zivanovic, K. S. Yee, and K. K. Mei, "A subgridding method for the time-domain finite-difference method to solve Maxwell's equations," *IEEE Transactions on Microwave Theory and Techniques*, vol. 39, pp. 471-479, 1991.

-
- [31] P. Thoma and T. Weiland, "A consistent subgridding scheme for the finite difference time domain method," *International Journal of Numerical Modelling-Electronic Networks Devices and Fields*, vol. 9, pp. 359-374, 1996.
- [32] S. Chaillou, J. Wiart, and W. Tabbara, "A subgridding scheme based on mesh nesting for the FDTD method," *Microwave and Optical Technology Letters*, vol. 22, pp. 211-214, 1999.
- [33] S. M. Wang, F. L. Teixeira, R. Lee, and J. F. Lee, "Optimization of subgridding schemes for FDTD," *IEEE Microwave and Wireless Components Letters*, vol. 12, pp. 223-225, 2002.
- [34] K. Xiao, D. J. Pommerenke, and J. L. Drewniak, "A three-dimensional FDTD subgridding algorithm based on interpolation of current density," *IEEE International Symposium on Electromagnetic Compatibility*, vol. 1, pp. 118-123, 2004.
- [35] J. H. Richmond, "Digital computer solutions of the rigorous equations for scattering problems," *Proceedings of the IEEE*, vol. 53, pp. 796- 804, 1965.
- [36] J. H. Richmond, "A wire-grid model for scattering by conducting bodies," *IEEE Transactions on Antennas and Propagation*, vol. 14, pp. 782-786, 1966.
- [37] R. F. Harrington, "Matrix methods for field problems," *Proceedings of the IEEE*, vol. 55, pp. 136-149, 1967.
- [38] R. F. Harrington, *Field computation by moment methods*. New York: The Macmillan Co., 1968.

-
- [39] L. Mendes and S. Antenor, "A tridimensional solenoidal basis function to analyze 3D scattering of homogeneous dielectrics using the method of moments," *SBMO/IEEE MTT-S International Microwave and Optoelectronics Conference Proceedings*, vol. 2, pp. 897-900, 1995.
- [40] S. Antenor and L. Mendes, "Method of moments with solenoidal basis functions: an approach to analyze the scattering by inhomogeneous dielectrics," *Third International Conference on Computation in Electromagnetics (Conf. Publ. No. 420)*, pp. 318-321, 1996.
- [41] D. Wilton and S. Govind, "Incorporation of edge conditions in moment method solutions," *IEEE Transactions on Antennas and Propagation*, vol. 25, pp. 845-850, 1977.
- [42] N. C. Albertsen, J. E. Hansen, and N. E. Jensen, "Computation of radiation from wire antennas on conducting bodies," *IEEE Transactions on Antennas and Propagation*, vol. 22, pp. 200-206, 1974.
- [43] E. H. Newman and D. M. Pozar, "Electromagnetic modeling of composite wire and surface geometries," *IEEE Transactions on Antennas and Propagation*, vol. 26, pp. 784-789, 1978.
- [44] M. E. Peters and E. H. Newman, "Method of moments analysis of anisotropic artificial media composed of dielectric wire objects," *IEEE Transactions on Microwave Theory and Techniques*, vol. 43, pp. 2023-2027, 1995.
- [45] S. M. Rao, D. R. Wilton, and A. W. Glisson, "Electromagnetic scattering by surfaces of arbitrary shape," *IEEE Transactions on Antennas and Propagation*, vol. 30, pp. 409-418, 1982.

-
- [46] A. J. Sangster and A. H. I. McCormick, "Theoretical design/synthesis of slotted waveguide arrays," *IEE Proceedings Microwaves, Antennas and Propagation*, vol. 136, pp. 39-46, 1989.
- [47] L. W. Li, C. P. Lim, and M. K. Leong, "Method of moments analysis of electrically large circular-loop antennas: non-uniform currents," *IEEE Antennas and Propagation Society International Symposium*, vol. 4, pp. 2542-2545, 1999.
- [48] L. W. Li, M. S. Yeo, and M. K. Leong, "Method of moments analysis of EM fields in a multilayered spheroid radiated by a thin circular loop antenna," *IEEE Transactions on Antennas and Propagation*, vol. 52, pp. 2391-2402, 2004.
- [49] S. N. Makarov, S. D. Kulkarni, A. G. Marut, and L. C. Kempel, "Method of moments solution for a printed patch/slot antenna on a thin finite dielectric substrate using the volume integral equation," *IEEE Transactions on Antennas and Propagation*, vol. 54, pp. 1174-1184, 2006.
- [50] J. T. Johnson, R. T. Shin, J. C. Eidson, L. Tsang, and J. A. Kong, "A method of moments model for VHF propagation," *Antennas and Propagation Society International Symposium*, vol. 1, pp. 362-365, 1997.
- [51] J. L. Hu, Z. P. Wu, H. McCann, L. E. Davis, and C. G. Xie, "Quasi-three-dimensional method of moments for analyzing electromagnetic wave scattering in microwave tomography systems," *IEEE Sensors Journal*, vol. 5, pp. 216-223, 2005.

Chapter 2

FDTD Technique for Field Truncation

2.1 Introduction

Over the past few years, finite-difference time-domain (FDTD) method [1] have become increasingly prevalent in the computational electromagnetic problems due to its simplicity, efficiency, robustness and versatility scheme for highly complex configuration in the computational domain. Generally, FDTD technique is the most well-known numerical method for the solution of problems in electromagnetic simulation ranging from RF to optical frequencies. It is considered to be one of the most powerful numerical techniques for solving partial differential equations of any kind. In addition, it can be utilized to solve the spatial as well as the temporal distributions of electric and magnetic fields in various media. In principle, FDTD is a method that divides the solution domain into finite discrete points and then replaces the partial differential equation with a set of difference equations. It has successfully been applied to many problems of propagation, radiation and scattering of electromagnetic waves such as antenna, radar, wireless communication system, high speed electronic, photonic, radiography, x-ray crystallography, bio-electromagnetic and geophysical imaging. A

good measure of its success lies in the fact that thousand of papers on the subject have been published in journals and international symposium, apart from the books and tutorials devoted to it. Moreover, much specific and general purpose commercial software is available on the market which further extends its appeal globally. Furthermore, three books are used as the main references to the recent FDTD research written by Taflove and Hagness [1], Taflove [2] and Kunz and Luebbers [3].

2.2 FDTD Updating Stencils

A pioneering way of describing the electromagnetic phenomena was introduced by James Clerk Maxwell in 1865 [4]. Later in 1873, he published an article called “Treatise on Electricity and Magnetism” in which the discoveries of Coulomb, Oersted, Ampere and Faraday were united into four refined constructed mathematical equations known as Maxwell’s equations. The differential time domain Maxwell’s equations in a linear medium are given by:

$$\frac{\partial B}{\partial t} = -\nabla \times E - J_m \quad (2.1)$$

$$\frac{\partial D}{\partial t} = \nabla \times H - J_e \quad (2.2)$$

B is the magnetic flux density in Wb/m^2 , D is the electric flux density in C/m^2 , E is the electric field in V/m and H is the magnetic field in A/m . J_m is the magnetic current density in V/m^2 and is defined to relate any magnetic loss to the field. J_e is the electric

current density in A/m² and is defined to relate any electric loss to the field. J_m and J_e are respectively given by:

$$J_m = \sigma^* \times H \quad (2.3)$$

$$J_e = \sigma \times E \quad (2.4)$$

σ^* is magnetic resistivity in Ω/m and σ is the electric conductivity in S/m. In materials with field-independent, direction-independent and frequency-independent electric and magnetic properties, the following proportions apply:

$$B = \mu \times H \quad (2.5)$$

$$D = \varepsilon \times E \quad (2.6)$$

μ is the magnetic permeability in H/m and ε is the electric permittivity in F/m. Inserting (2.3) and (2.5) to (2.1) and dividing by μ gives:

$$\frac{\partial H}{\partial t} = \frac{1}{\mu} \left(-\nabla \times E - \sigma^* H \right) \quad (2.7)$$

$\sigma^* H$ is the magnetic losses which may exist inside the medium. Inserting (2.4) and (2.6) to (2.2) and dividing by ε gives:

$$\frac{\partial E}{\partial t} = \frac{1}{\varepsilon} (\nabla \times H - \sigma E) \quad (2.8)$$

σE is the electric losses which may exist inside the medium. In Cartesian coordinates, equations (2.7) and (2.8) yield the following six scalar equations:

$$\frac{\partial H_x}{\partial t} = \frac{1}{\mu} \left(\frac{\partial E_y}{\partial z} - \frac{\partial E_z}{\partial y} - \sigma^* H_x \right) \quad (2.9)$$

$$\frac{\partial H_y}{\partial t} = \frac{1}{\mu} \left(\frac{\partial E_z}{\partial x} - \frac{\partial E_x}{\partial z} - \sigma^* H_y \right) \quad (2.10)$$

$$\frac{\partial H_z}{\partial t} = \frac{1}{\mu} \left(\frac{\partial E_x}{\partial y} - \frac{\partial E_y}{\partial x} - \sigma^* H_z \right) \quad (2.11)$$

$$\frac{\partial E_x}{\partial t} = \frac{1}{\varepsilon} \left(\frac{\partial H_z}{\partial y} - \frac{\partial H_y}{\partial z} - \sigma E_x \right) \quad (2.12)$$

$$\frac{\partial E_y}{\partial t} = \frac{1}{\varepsilon} \left(\frac{\partial H_x}{\partial z} - \frac{\partial H_z}{\partial x} - \sigma E_y \right) \quad (2.13)$$

$$\frac{\partial E_z}{\partial t} = \frac{1}{\varepsilon} \left(\frac{\partial H_y}{\partial x} - \frac{\partial H_x}{\partial y} - \sigma E_z \right) \quad (2.14)$$

A space point in a rectangular grid is defined from Yee's original notation [5] as:

$$(i, j, k) = (i\Delta x, j\Delta y, k\Delta z) \quad (2.15)$$

Let F denote any function of discrete space and time given by:

$$F(i\Delta x, j\Delta y, k\Delta z, n\Delta t) \equiv F_{i,j,k}^n \quad (2.16)$$

Δx , Δy and Δz are the grid space increments in x , y and z directions respectively, and Δt is the time increment. Using a central finite-difference approximation, space and time derivatives of F can be written as:

$$\frac{\partial F}{\partial x} = \frac{F_{i+1/2,j,k}^n - F_{i-1/2,j,k}^n}{\Delta x} + O(\Delta x)^2 \quad (2.17)$$

$$\frac{\partial F}{\partial t} = \frac{F_{i,j,k}^{n+1/2} - F_{i,j,k}^{n-1/2}}{\Delta t} + O(\Delta t)^2 \quad (2.18)$$

In equation (2.17), $O(\Delta x)^2$ is the error term that represents all the remaining terms in a Taylor series expansion. It is known as a central finite difference scheme in space with second-order accuracy. Similarly, (2.18) is second-order accurate in time. Applying Yee's finite-difference scheme to (2.9) gives:

$$\frac{H_x|_{i,j,k}^{n+1/2} - H_x|_{i,j,k}^{n-1/2}}{\Delta t} = \frac{1}{\mu_{i,j,k}} \left(\frac{E_y|_{i,j,k+1/2}^n - E_y|_{i,j,k-1/2}^n}{\Delta z} - \frac{E_z|_{i,j+1/2,k}^n - E_z|_{i,j-1/2,k}^n}{\Delta y} - \sigma_{i,j,k}^* H_x|_{i,j,k}^n \right) \quad (2.19)$$

The $H_x|_{i,j,k}^n$ field component in (2.19) is evaluated at time step n . However, the value of $H_x|_{i,j,k}^n$ at time step n is not available and hence the following interpolated approximation is used:

$$H_x|_{i,j,k}^n = \frac{H_x|_{i,j,k}^{n+1/2} + H_x|_{i,j,k}^{n-1/2}}{2} \quad (2.20)$$

By substituting equation (2.20) in (2.19), leaving $H_x|_{i,j,k}^{n+1/2}$ on the left hand side and passing the all remaining terms to the right, assuming cubical FDTD cells are used, the finite difference updating equation for the magnetic and electric field components can be derived as:

$$H_x|_{i,j,k}^{n+1/2} = D_{a,H_x}|_{i,j,k} H_x|_{i,j,k}^{n-1/2} + D_{b,H_x}|_{i,j,k} \left(\frac{E_y|_{i,j,k+1/2}^n - E_y|_{i,j,k-1/2}^n}{\Delta z} + \frac{E_z|_{i,j-1/2,k}^n - E_z|_{i,j+1/2,k}^n}{\Delta y} \right) \quad (2.21)$$

$$H_y|_{i,j,k}^{n+1/2} = D_{a,H_y}|_{i,j,k} H_y|_{i,j,k}^{n-1/2} + D_{b,H_y}|_{i,j,k} \left(\frac{E_z|_{i+1/2,j,k}^n - E_z|_{i-1/2,j,k}^n}{\Delta x} + \frac{E_x|_{i,j,k-1/2}^n - E_x|_{i,j,k+1/2}^n}{\Delta z} \right) \quad (2.22)$$

$$H_z|_{i,j,k}^{n+1/2} = D_{a,H_z}|_{i,j,k} H_z|_{i,j,k}^{n-1/2} + D_{b,H_z}|_{i,j,k} \begin{pmatrix} E_x|_{i,j+1/2,k}^n - E_x|_{i,j-1/2,k}^n \\ + E_y|_{i-1/2,j,k}^n - E_y|_{i+1/2,j,k}^n \end{pmatrix} \quad (2.23)$$

$$E_x|_{i,j,k}^{n+1} = C_{a,E_x}|_{i,j,k} E_x|_{i,j,k}^n + C_{b,E_x}|_{i,j,k} \begin{pmatrix} H_z|_{i,j+1/2,k}^{n+1/2} - H_z|_{i,j-1/2,k}^{n+1/2} \\ + H_y|_{i,j,k-1/2}^{n+1/2} - H_y|_{i,j,k+1/2}^{n+1/2} \end{pmatrix} \quad (2.24)$$

$$E_y|_{i,j,k}^{n+1} = C_{a,E_y}|_{i,j,k} E_y|_{i,j,k}^n + C_{b,E_y}|_{i,j,k} \begin{pmatrix} H_x|_{i,j,k+1/2}^{n+1/2} - H_x|_{i,j,k-1/2}^{n+1/2} \\ + H_z|_{i-1/2,j,k}^{n+1/2} - H_z|_{i+1/2,j,k}^{n+1/2} \end{pmatrix} \quad (2.25)$$

$$E_z|_{i,j,k}^{n+1} = C_{a,E_z}|_{i,j,k} E_z|_{i,j,k}^n + C_{b,E_z}|_{i,j,k} \begin{pmatrix} H_y|_{i+1/2,j,k}^{n+1/2} - H_y|_{i-1/2,j,k}^{n+1/2} \\ + H_x|_{i,j-1/2,k}^{n+1/2} - H_x|_{i,j+1/2,k}^{n+1/2} \end{pmatrix} \quad (2.26)$$

It can be seen that the coefficients on the left hand side are referred to as Yee's updating coefficients. The electric field coefficients are given by:

$$C_a|_{i,j,k} = \left(1 - \frac{\sigma_{i,j,k} \Delta t}{2\varepsilon_{i,j,k}} \right) / \left(1 + \frac{\sigma_{i,j,k} \Delta t}{2\varepsilon_{i,j,k}} \right) \quad (2.27)$$

$$C_{b_p}|_{i,j,k} = \left(\frac{\Delta t}{\varepsilon_{i,j,k} \Delta_p} \right) / \left(1 + \frac{\sigma_{i,j,k} \Delta t}{2\varepsilon_{i,j,k}} \right) \quad (2.28)$$

The magnetic updating coefficients can be written as:

$$D_a|_{i,j,k} = \left(1 - \frac{\sigma_{i,j,k}^* \Delta t}{2\mu_{i,j,k}}\right) \bigg/ \left(1 + \frac{\sigma_{i,j,k}^* \Delta t}{2\mu_{i,j,k}}\right) \quad (2.29)$$

$$D_{b_p}|_{i,j,k} = \left(\frac{\Delta t}{\mu_{i,j,k} \Delta_p}\right) \bigg/ \left(1 + \frac{\sigma_{i,j,k}^* \Delta t}{2\mu_{i,j,k}}\right) \quad (2.30)$$

The subscript p can be x , y or z and Δ_p is the cell size in the p -direction. Assuming the structure under investigation contains different types of material such as dielectric or magnetic, electric and magnetic field updating coefficients can be easily calculated from equations (2.27) to (2.30) before the FDTD time stepping algorithm starts. The orientation of the fields in Figure 2.1 is known as the FDTD lattice or Yee cell. The magnetic and electric fields are located on the faces and the edges of the cube respectively. Each electric field vector component is surrounded by four circulating magnetic field vector components and vice versa. Both the electric and magnetic field vector components are located half a cell from each other. In addition, this arrangement permits easy implementations of the central finite difference approximations and the integral form of the Faraday's law and the Ampere's law. The system of difference equations is solved at the nodes. Figure 2.2 illustrates the typical relationship between field components within a quarter of a cell and on a plane distinctly helpful when handling boundary conditions of a closed region.

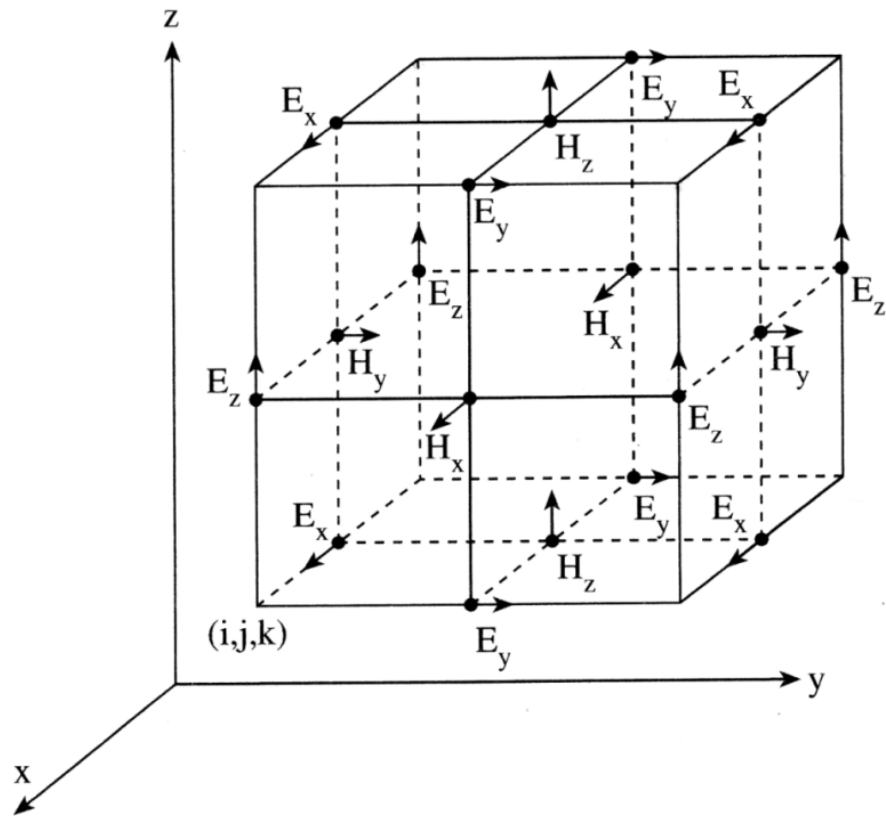


Figure 2.1: The electric and magnetic field components distribution on the FDTD lattice [6].

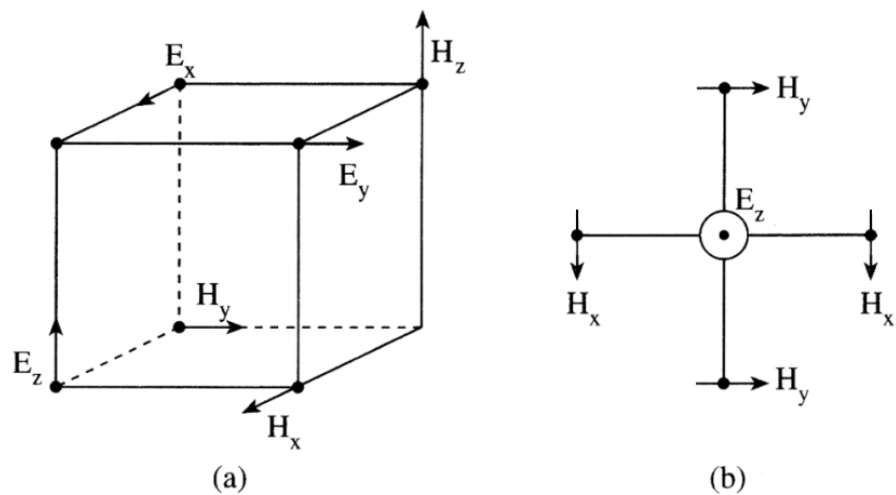


Figure 2.2: Relationship between field components: (a) within a quarter of a unit cell, (b) on a plane [6].